Supplementary Material to: "Meeting Summary: Exploring Cloud Dynamics with Cloud Model 1 and 3D Visualization – insights from a University Modeling Workshop"

Lisa Schielicke[1], Yidan Li[1], Jerome Schyns[1], Aaron Sperschneider[1], Jose Pablo Solano Marchini[1], and Christoph Peter Gatzen[2]

[1]University Bonn, Institute of Geosciences, Department Meteorology, Auf dem Hügel 20, 53121 Bonn, Germany
[2]European Severe Storms Laboratory e.V. (ESSL), c/o DLR, Münchener Str. 20 82234 Wessling, Germany

Correspondence: Lisa Schielicke (schieli@zedat.fu-berlin.de)

1 Students projects

This supplementary material aims to document the students' projects of own choice. The projects will be presented in alphabetical order based on the students' first names.

1.1 Aaron Sperschneider's (AS) project: influence of topography on deep moist convection under weak and mesoscale lifting conditions

AS focus on the influence of the local topography on deep moist convection. Being an active storm chaser in western Germany, he wanted to reproduce his observation that storms over the mountains tend to be more intense in some situations, and that the intensity difference is dependent on the local lifting mechanism. He started to work in this field for his Bachelor's thesis using the limited-area numerical weather prediction model COSMO-DE provided by the German Weather Service (Deutscher Wetterdienst, DWD) with a grid spacing of 2.8 km and a temporal resolution of 15 min. In his thesis, he reproduced the convective development on two different cases, one with very local, weak lifting and one with more widespread and stronger mesoscale lifting. To answer the initial research question, AS did a comparison of the maximum updraft intensity of the convective storms using the distributions of updraft speed and precipitation rate of the simulated convective cells. He found that in situations with weaker lift, storms over the mountains (terrain height below 1000 m) had a tendency to be more intense compared to storms forming over the lowlands. However, in the case of mesoscale lift, the difference between storms over mountains and lowlands was small. This result did not only reflect his observations, it can also be used for nowcasting purposes and shows the importance of the local topography for convective storms development, in case of rather small mountains.

The CM1 course gave AS the possibility to study the storms of the presented cases in greater detail with a higher spatio-temporal resolution. Using CM1 on the Bonna HPC cluster, AS tested different model resolutions ranging from 1000 m to 250 m. The model was initialized with a verticl profile obtained from real observations of rawinsonde data (https://opendata.dwd.de/ of DWD) of one of the two cases (weak forcing case) and compared to model simulations initialized with the Weisman-Klemp
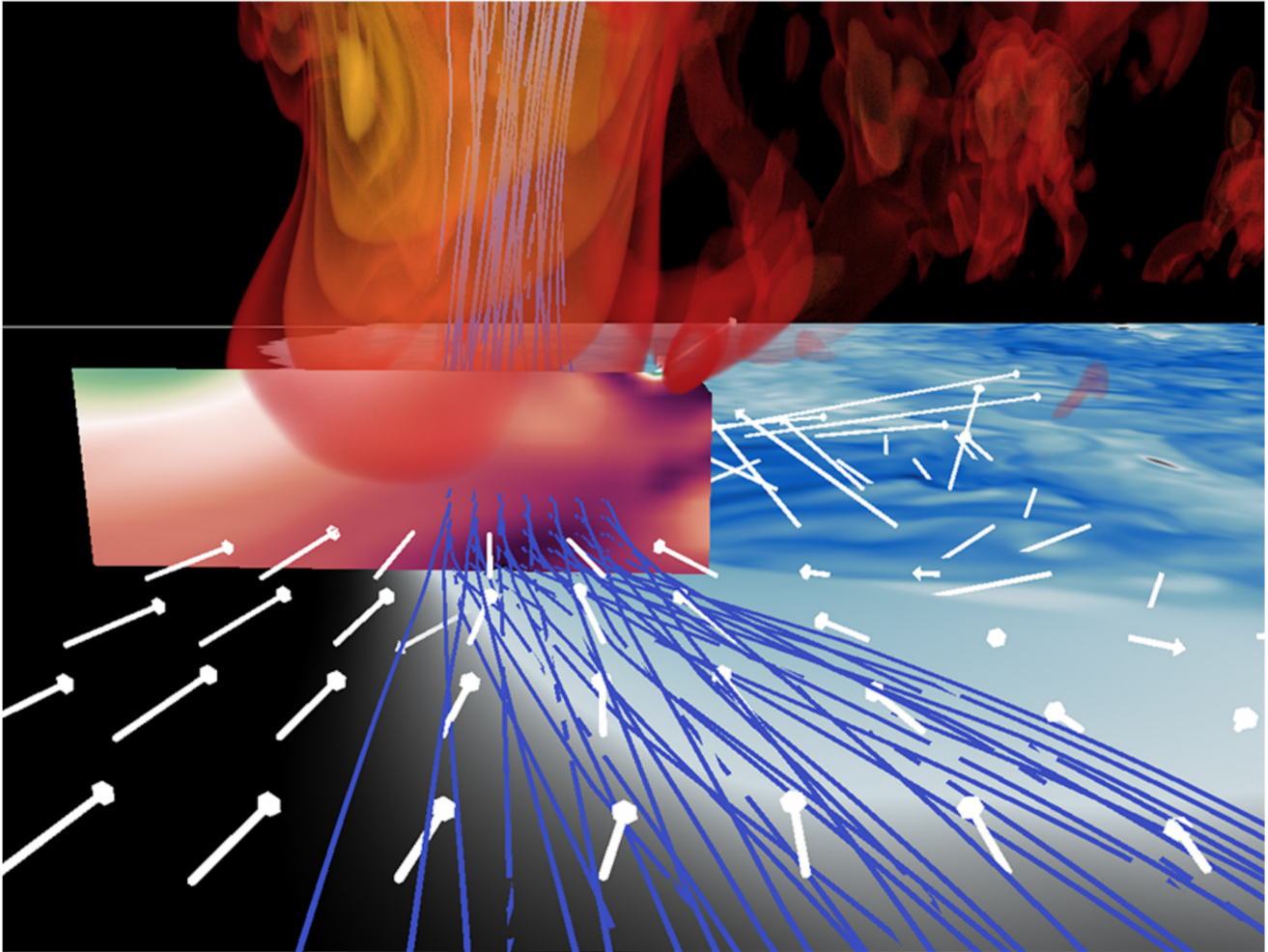
Figure 1. 3D-visualization of the supercell forming in the simulation with the Weisman-Klemp sounding (simulation without terrain). The volume (red to yellow) shows the updraft velocity in 10 ms-1 intervals, starting at 10 ms-1. Negative values of the potential temperature perturbation in the lowest model level are shown in blue to visualize the cold pool. The cross section shows the x-component of vorticity up to 3 km height. Streamlines (blue) and 3d-vorticity vectors (white) show properties of the wind field. Note, the vorticity vectors align with the streamlines (streamwise vorticity) closer to the updraft, especially within the gradient of potential temperature perturbation. Figure was plotted by Aaron Sperschneider using VAPOR.

supercell sounding (Weisman and Klemp, 1982) leading to a long-lived supercell in contrast to the single cells simulated by CM1 in the real rawinsonde data. AS again plotted the development of the maximum updraft intensity and precipitation rate and compared it to the COSMO-DE results.

25   Moreover, AS worked with VAPOR, ParaView, and Ncview visualization software to show the storm structure, including the development of up- and downdrafts, clouds, precipitation, and vortex lines (see Figs. 1 and 2). While Fig. 1 the relation
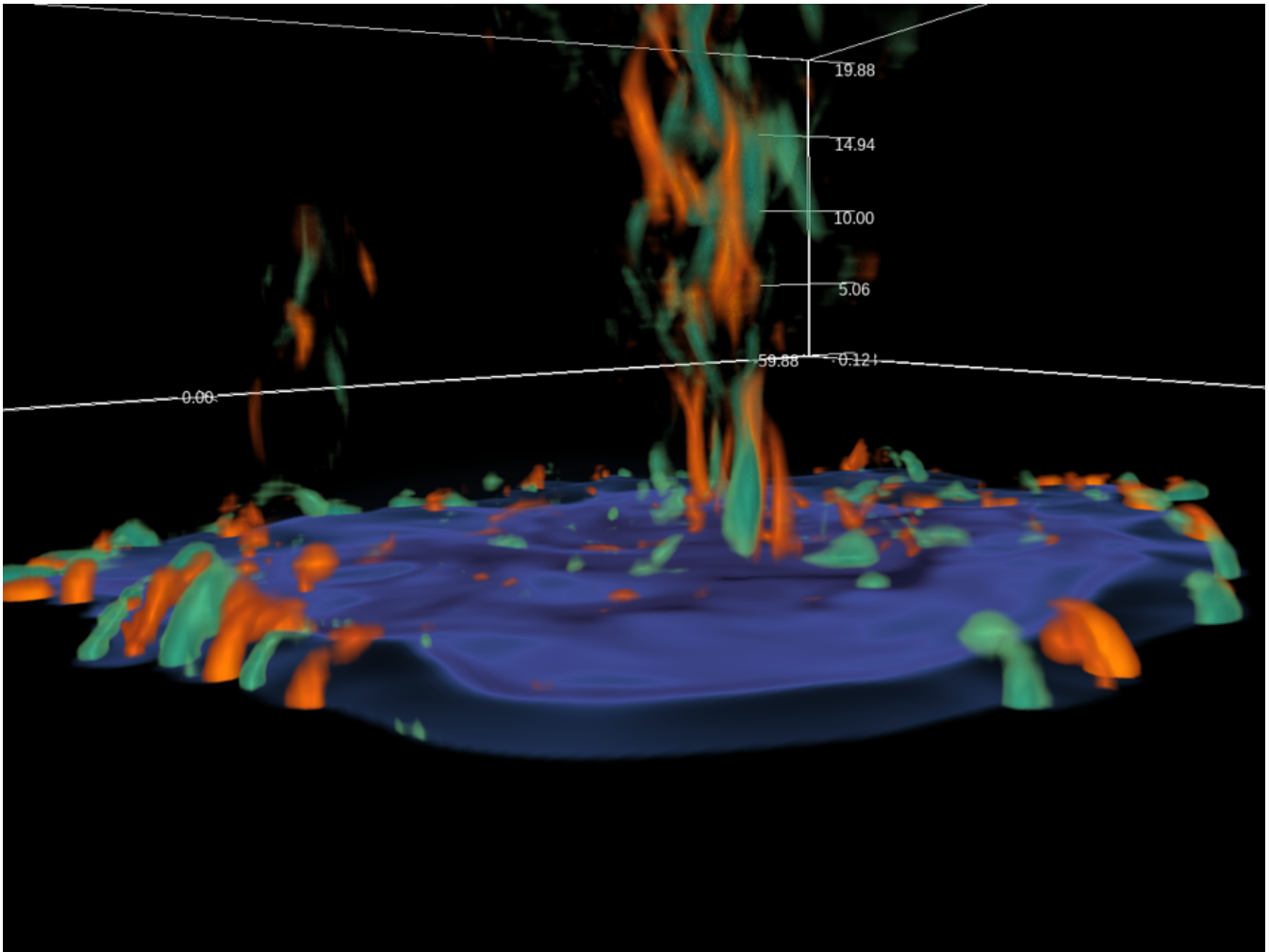
Figure 2. 3D-visualization of the cold pool formed by short lived cells in the weak dynamic case obtained from real rawinsonde data (simulation without terrain is shown at a simulation time of 67.5 min). Negative potential temperature perturbation in the lowest model-level is shown in blue (-0.5 K isotherm). The volume shows the vertical component of vorticity. Values larger than $0.013s^{-1}$ are shown in orange and values smaller than $-0.013s^{-1}$ are shown in turquoise. Positive and negative vorticity maxima form along the gust front. Figure was plotted by Aaron Sperschneider using VAPOR.

between updraft, streamlines and vorticity in the fully-developed Weisman-Klemp supercell case, Fig. 2 shows the relation between downdraft and the development of vorticity patches at the edges of a coldpool.
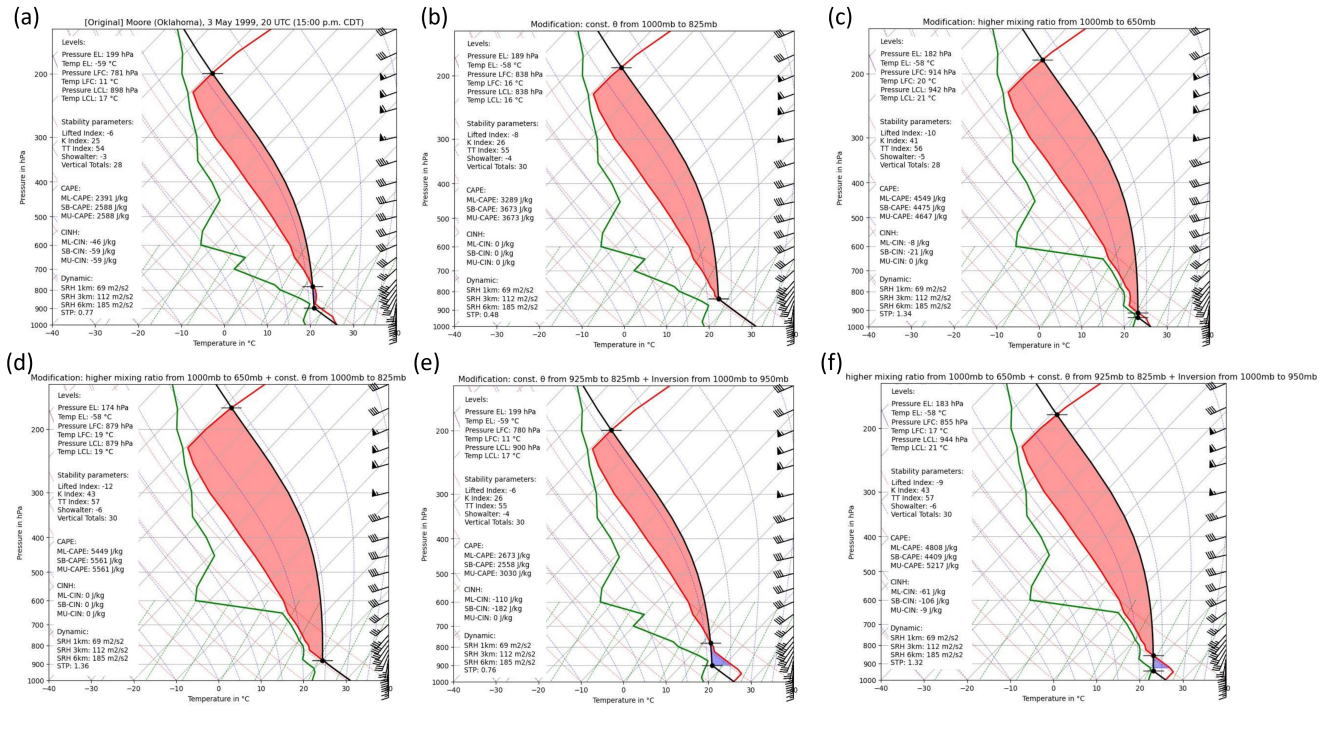
Figure 3. Vertical profile of the Moore (Oklahoma) tornado case derived from ERA5 reanalysis data. (a) without modifications (original); (b) $\theta = const.$ between 1000 hPa and 825 hPa, taking the value at $p = 825$ hPa; (c) increased mixing ratio q_v in the lowest 350 hPa; (d) Combination of soundings b. and c.; (e) $\theta = const$ between 925 hPa and 825 hPa, taking the value at $p = 825$ hPa, and an temperature T inversion below with $T = const$ between 1000 hPa and 950 hPa; (f) Combination of Soundings e. and c. Profiles were plotted by Jerome Schyns.

1.2 Jerome Schyn's (JS) project: Study of different triggers and modified soundings of the Moore/Oklahoma tornado outbreak on 3 May 1999

JS studied different combinations of trigger mechanisms and (modified) soundings of the Moore/Oklahoma (USA) tornado outbreak that occurred on 3 May 1999. On that day an outbreak of severe tornadic supercells formed in the Great Plains; one of them spawned a devastating F5 tornado that hit the cities Bridge Creek, Oklahoma City and Moore (Speheger et al., 2002). The tornado crossed four counties and lasted more than an hour starting at 18:26 CDT on 3 May (23:26-00:48 UTC). Its path length was about 60 km with a maximum width of approximately 1.6 km. The associated convection was first observed in visible imagery at 15:15 CDT (20:15 UTC) in the southwest of Oklahoma (USA) in the vicinity of a dryline (Bikos et al., 2002). This first convection rapidly evolved and produced the first right-moving supercell after a storm split (Thompson and Edwards, 2000).

Table 1. Results of JS's simulations of various (modified) 3-May-1999 Moore/Oklahoma tornado outbreak soundings in dependence on different initiations (triggers) based on a visual analysis of the simulated data using ncview. Different background color indicates convective type as well as cases that did not initiate. This project was done by Jerome Schyns.

Sounding ⟶ Trigger ↓	Original	θ =const.	larger q_v	θ =const. & larger q_v	θ =const. & inversion	θ =const. & larger q_v & inversion
1 warm bubble (iinit=1)	no initiation	no initiation	supercells	supercells (system)	no initiation	supercells (system)
2 warm bubbles (own definition)	no initiation	no initiation	supercells (system)	supercells (system)	no initiation	supercells (system)
3 warm bubbles (iinit=3)	no initiation	no initiation	supercells (system)	supercells (system)	no initiation	supercells (system)
cold pool (iinit=2)	no initiation	single cells (postfrontal)	linear system+ poss. supercell	linear system	no initiation	linear system
dry line (iinit=4)	development of clusters	linear system	development of clusters	development of clusters	linear system	linear system
outflow boundary (iinit=5)	no initiation	single cell (short-lived)	supercells (late development)	supercells (system)	no initiation	supercells (system)
forced convergence (iinit=9)	no initiation	single cell (short-lived)	supercells	supercells (system)	no initiation	supercells (system)

Given that CM1 model simulations rely on a single representative vertical profile for initialization, JS decided to extract this sounding from ERA 5 reanalysis data (Hersbach et al., 2020) due to the absence of available observational soundings. He extracted potential temperature, mixing ratio, and the horizontal wind components at all available pressure levels at a location oft $-97.49°$ longitude and $35.34°$ latitude at 15:00 CDT (20:00 UTC) on 3 May 1999 from the ERA5 reanalysis data (see Fig. 3). Subsequently, he modified the sounding data in order to study the influence of changes to the environment on the storm appearance. He derived the following setup of six initial soundings:

a. Original sounding (no modifications, plotted in Fig. 3a).

b. Constant potential temperature θ between 1000 hPa and 825 hPa, taking the value at $p = 825$ hPa (Fig. 3b).

c. (Subjectively-chosen) Increase of the mixing ratio q_v in the lowest 350 hPa (Fig. 3c).

d. Combination of b. and c. (Fig. 3d)

e. Constant potential temperature θ between 925 hPa and 825 hPa, taking the value at $p = 825$ hPa, and an temperature inversion below. Between 1000 hPa and 950 hPa, the atmosphere is isothermal (Fig. 3e).

f. Combination of e. and c. (Fig. 3f)

Numerous preconfigured triggers are available in CM1, which can be selected by varying the values in the namelist variable *iinit*. JS tested different triggers such as one warm bubble (namelist variable iinit=1), a cold pool (iinit=2), a line of three warm bubbles (iinit=3), a dry line (iinit=4), an outflow boundary (iinit=5) and a forced low-level convergence (after Loftus et al., 2008, iinit=9). Additionally, JS wrote his own modification of a line of two bubbles with a distance of 70 km based on iinit=3. As a general setup, the preconfigured supercell setup was used and initiated by the modified soundings. This setup has a horizontal grid spacing of 1000 m and a vertical one of 500 m and covers a domain of 150x150x40 grid points (length x width x height). The output frequency was set to 1000 s. JS's results for different combinations of triggers and soundings are listed in Table 1.
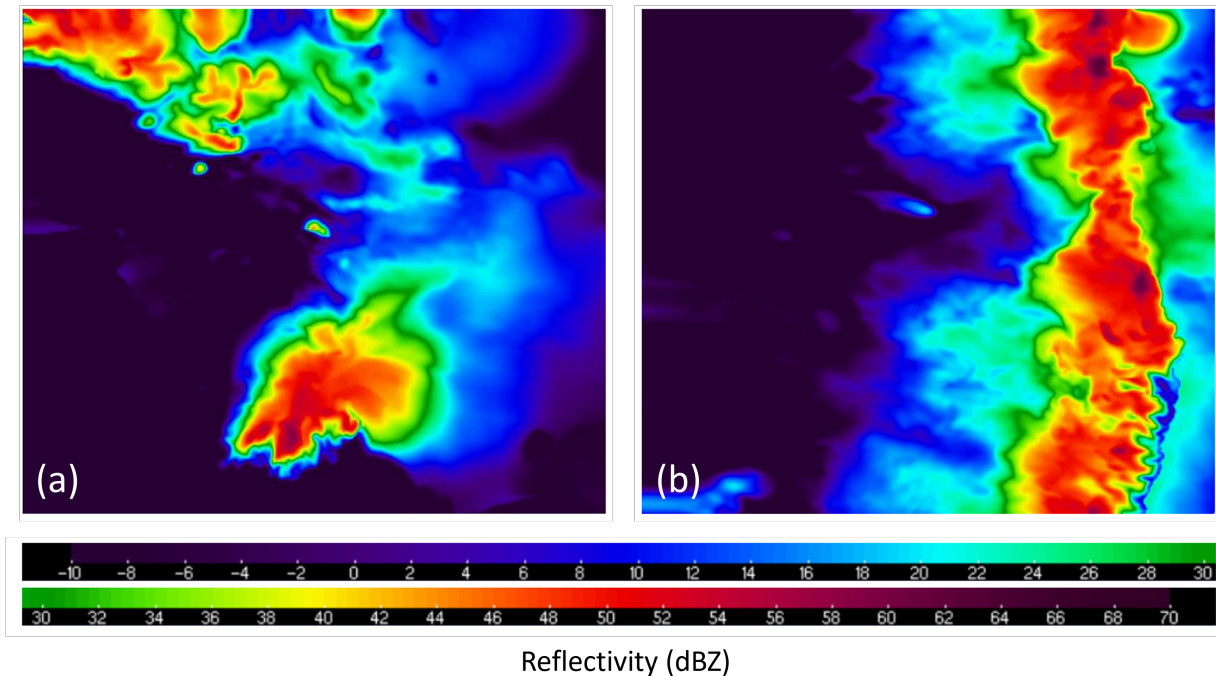

Reflectivity (dBZ)

Figure 4. Reflectivity at 250 m height after $t = 21600$ s of the simulation; convection was initiated by one warm bubble. (a) Modified sounding with higher mixing ratio between 1000 hPa and 650 hPa (Sounding c.). (b) Modified sounding with higher mixing ratio between 1000 hPa and 650 hPa; constant potential temperature between 925 hPa and 825 hPa and an (isothermal) inversion between 1000 hPa and 950 hPa (Sounding f.)
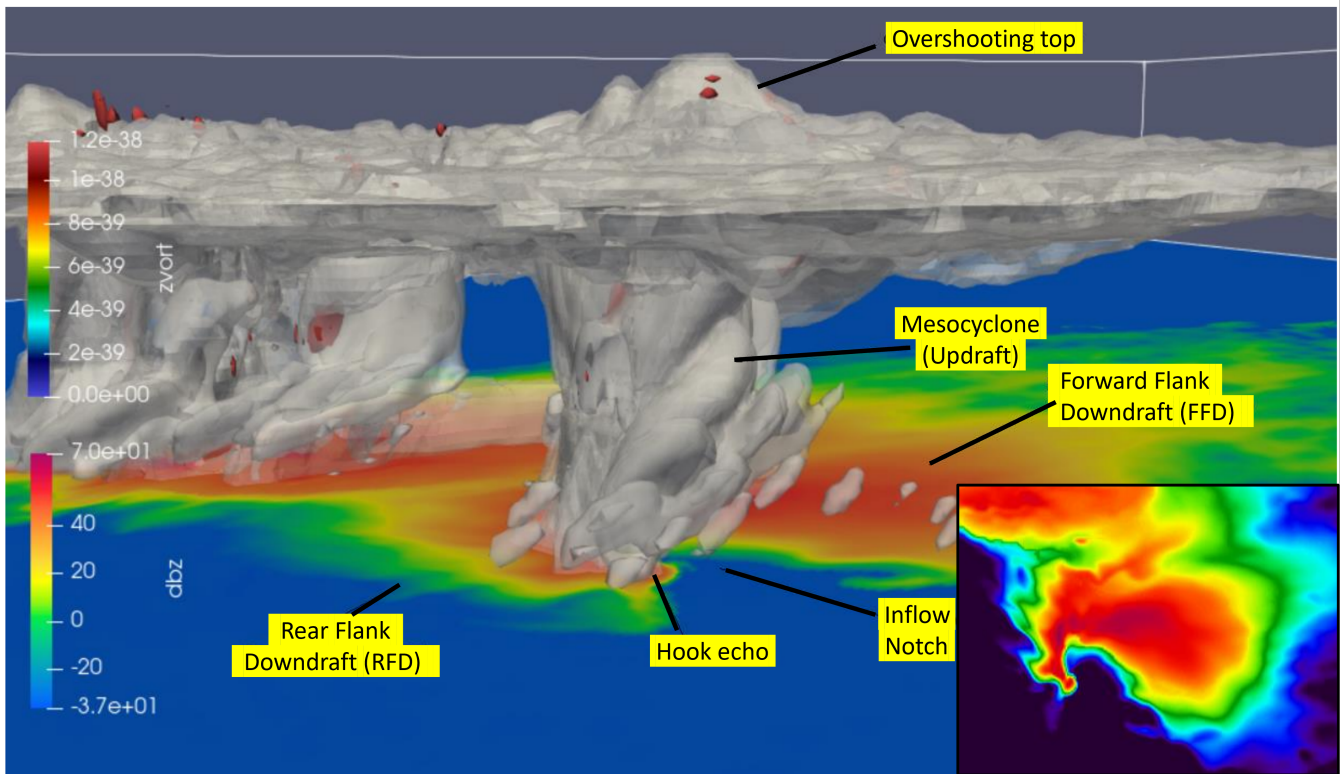
Figure 5. 3D visualization of the right-moving supercell with its typical characteristics at $t = 9900$ s into the simulation. Color-shaded on the surface of the plot is the reflectivity (in dBZ) at a height of 250 m. The inset also shows the reflectivity at 750 m as a 2D plot. Whitish colors represent the cloud composed of the mixing ratios of cloud particles (q_c), graupel (q_g) and ice (q_i). Inside the clouds, colored shadings represent positive vertical vorticity ζ surfaces with values of $\zeta = 0.03 s^{-1}$ and $\zeta = 0.05 s^{-1}$. Figure was plotted using ParaView (3D) and ncview (2D) by Jerome Schyns.

60   JS showed that the appearance of the convection strongly depends on the initiation mechanisms as well as the sounding details (see Table 1 and Fig. 4). Interestingly, the original sounding did not lead to the initiation of cells at all (except for the dryline, see Table 1). This finding is important, as it might discourage students or researchers aiming to examine supercells through reanalysis data or observational vertical profiles, yet facing challenges in initiating cells. JS's project emphasizes the potential necessity of modifying soundings to attain "reasonable" outcomes. Furthermore, his results might have potential

65   implications for reanalysis data sets providers, suggesting potential inadequacies in representing the boundary layer (e.g., excessive dryness). However, this would need further investigation.

     Additionally to the 1000 m grid spacing runs, JS studied higher-resolved simulations with an isotropic grid spacing of 500 m in a domain of 700 x 700 x 40 grid points and an output frequency of 900 s (15 min) in order to study the three-dimensional structure of the cells. A snapshot of the simulated supercell based on the initiation with one warm bubble and an elevated

70   mixing ratio in the lowest levels (Sounding c.) is given in Fig. 5. The image is taken at 9900 s (2.75 h) runtime. The cell split
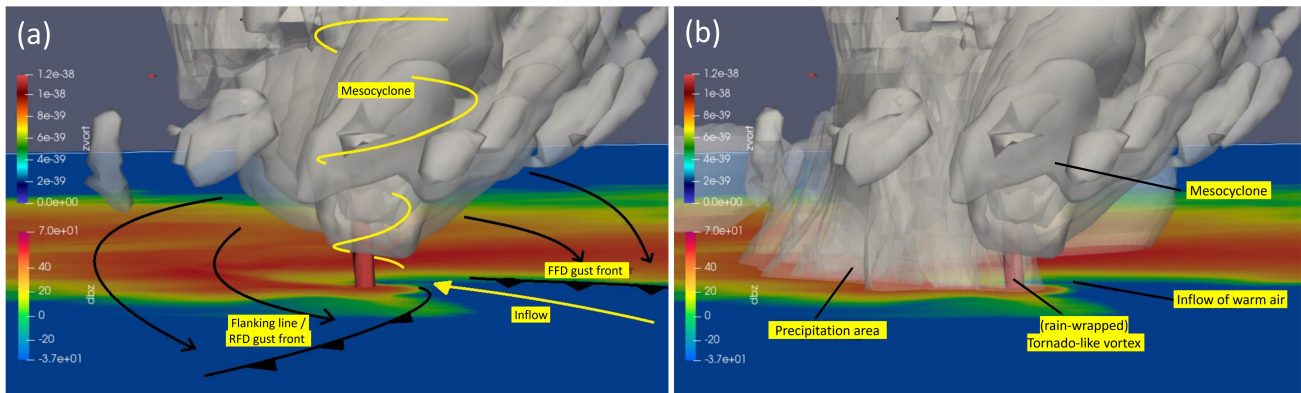
Figure 6. 3D visualization of the right-moving supercell at $t = 9900$ s. (a) Mesocyclonic rotation and possible tornado-like vortex represented by high values of positive vertical vorticity (red surface in the center of the figure); (b) Mixing ratio of rain (q_R) is added; All other variables as in Fig. 5. Figure was plotted using ParaView by Jerome Schyns.

already occurred and the right-mover is in the center of the plot (Fig. 5). The right-mover shows the typical characteristics of a supercell such as the rotating updraft (mesocyclone), the rear- and forward-flank downdrafts and an overshooting top. The reflectivity at 750 m (2D view) shows a pronounced hook echo (inset in Fig. 5).

Fig. 6 shows the lower parts of the right-moving supercell at the same time step in more detail and from a slightly different angle. The image shows the existence of a tornado-like vortex represented by high values of positive vertical vorticity ζ ($\zeta = 0.03s^{-1}$, outer reddish tube in Fig. 6 and $\zeta = 0.05s^{-1}$ as darker reddish surface) that reaches down to the lowest model level (250 m) and is located in the region of the hook echo. Correspondingly, the lowered wall cloud and helical appearance of the low-level mesocyclone are visible.

Overall JS's project shows the combination of the three workshop key aspects: The gained knowledge about severe convective storms is reflected by searching for a useful visualization to interpret the model data. Furthermore, JS's results highlight the significance of initiation mechanisms and sounding parameters on convection patterns, with potential implications for studying supercells using reanalysis data or observational profiles.

1.3 Jose Pablo Solano Marchini's (JPSM) project: Comparing the development and microphysical composition of high-humidity/classic/low-humidity supercells

JPSM's project focuses on the differences between supercells in environments characterized by varying moisture (low-humidity, classic and high-humidity supercells) with and without terrain regarding their development and microphysical composition. Therefore, he conducted supercell simulations based on CM1's pre-configured supercell setup with modified soundings visualizing the results with ParaView. JPSM compared different scenarios that were initialized with systematically-modified input soundings: (1a) classic Weisman-Klemp supercell sounding (Weisman and Klemp, 1982) without and (1b) with a modification

Table 2. Lowest height levels of Weisman and Klemp's supercell sounding (Theta, horizontal wind speeds in x- and y-direction (U,V)) and modified (Pablos data) - Height levels and corresponding theta and mixing ratio values of the original Weisman and Klemp sounding (columns 1, 2, and 4) as well as modified values of moisture (columns 3 and 5) and u- and v-wind vectors (columns 6 and 7).

Height (m)	θ (K)	q (g/kg) high-humidity case (HH)	q (g/kg) original case (OH)	q (g/kg) low-humidity case (LH)	U-wind (m/s)	V-wind (m/s)
250	300.3	15.0	14.0	13.0	-12.4	-1.6
750	301.3	15.0	14.0	13.0	-11.3	0.9
1250	302.5	14.8	13.8	12.8	-9.4	2.8
1750	303.9	12.3	11.3	10.3	-6.9	3.9
2250	305.3	9.8	9.3	8.8	-4.0	4.0
2750	306.8	7.5	7.5	7.5	-1.0	4.0
...	...	...	...	...	...	...

to the upper level winds and two adjusted Weisman-Klemp supercell sounding to account for (2) low- and (3) high-humidity supercells by modifying systematically the low level humidity (see Table 3). These four soundings were run with and without terrain. Thereby JPSM focused on the region around Veneto, Italy including parts of the Alps, a region known as "a hot spot in Europe for tornadoes" (De Martin et al., 2023). The terrain data is based on the Continental Europe Digital Terrain Model with a raster resolution of 30 meters available at the OpenTopography portal (Hengl et al., 2022). To get stable simulations, the terrain was heavily smoothed by a script provided during the course. However, results for the terrain runs will not be shown here. Furthermore, the impact of the upper-level wind shear modification (sounding 1b) was limited in the simulations, hence we do not show any results here.

Using ParaView, JPSM compared the simulated radar reflectivity (dBZ) and the mixing ratios of rain q_R and graupel q_G of the first two hours of the supercell simulations to understand the differences between the developing supercells. He observed differences in the 2D (Fig. 7) and 3D (Fig. 8) structure and microphysical composition of the supercells comparing the same time steps after the simulation started. While high-humidity and classic environments show only minor differences with respect to reflectivity and size (Fig 7a,b and 7d,e as well as Fig. 8a,b and 8d,e), the graupel mixing ratio within the inner mesocyclone of the high humidity supercell was notably higher (Fig. 7c and 7f as well as Fig. 8c and 8f), implying the importance of initial humidity in the accretion process when terrain is not considered. Furthermore, JPSM observed accelerated supercell development (high-humidity case) in the presence of mountains (not shown) suggesting that terrain impacts supercell formation probably by affecting wind patterns, temperature and moisture distributions, atmospheric instability, and therefore the severe weather potential.

In contrast, the supercell, that formed under low humidity conditions, exhibits distinct differences. After one hour, the low humidity supercell is only half the size of the high humidity supercell, and its mixing ratios of rain and graupel were much lower as can be seen in the 2d cross sections at 1.5 km height (Fig 7g-i) as well as in the general 3D structure of the cells

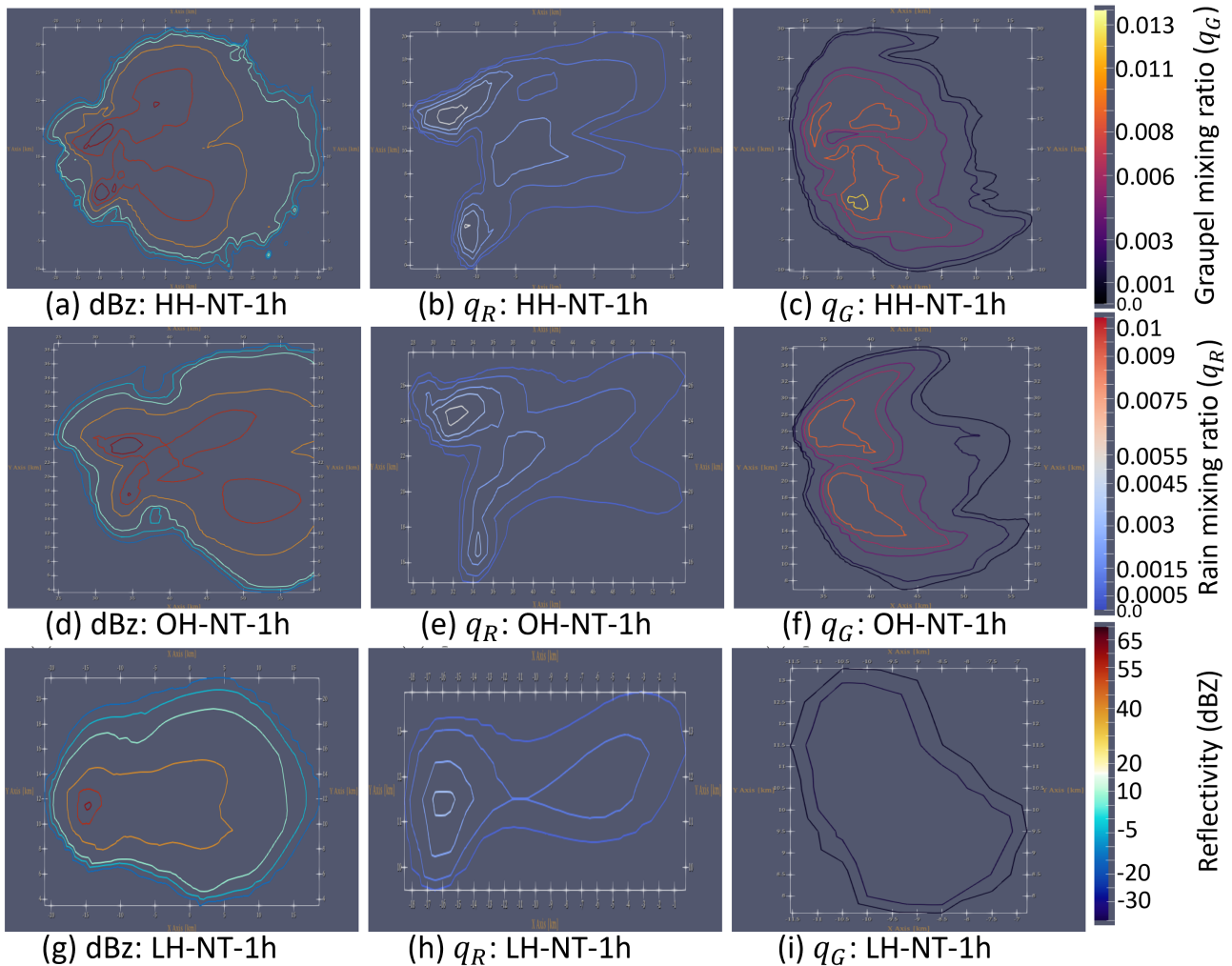**Figure 7.** Plane view of (left column) reflectivity (dBZ, contours: $-14.26, -3.52, 8.45, 39.72, 53.90$ and 59.89 dBZ), (middle column) mixing ratio of rain (q_R in kg/kg, contours: $0.0006, 0.0012, 0.0024, 0.0035, 0.0051$ and 0.0069 kg/kg) and (right column) mixing ratio of graupel (q_G in kg/kg, contours: $0.0010, 0.0015, 0.0044, 0.0061, 0.0088$ and 0.0120 kg/kg). Reflectivity is plotted at a height of 2.5 km; mixing ratios are plotted at a height of 1.5 km. (Top row) high-humidity (HH) (middle row) original humidity (OH), and (bottom row) low-humidity (LH) simulations without terrain (NT) for 1 hour (1h) into the simulation. Figure plotted with ParaView by Jose Pablo Solano Marchini.

(Fig 8g-i). The development is slower in the low humidity environment. Comparable values to the other two simulations are reached after two hours. These differences underscore the role of humidity in precipitation processes within supercells, where higher humidity levels lead to stronger updrafts, condensation, and graupel formation, potentially resulting in heavier rainfall
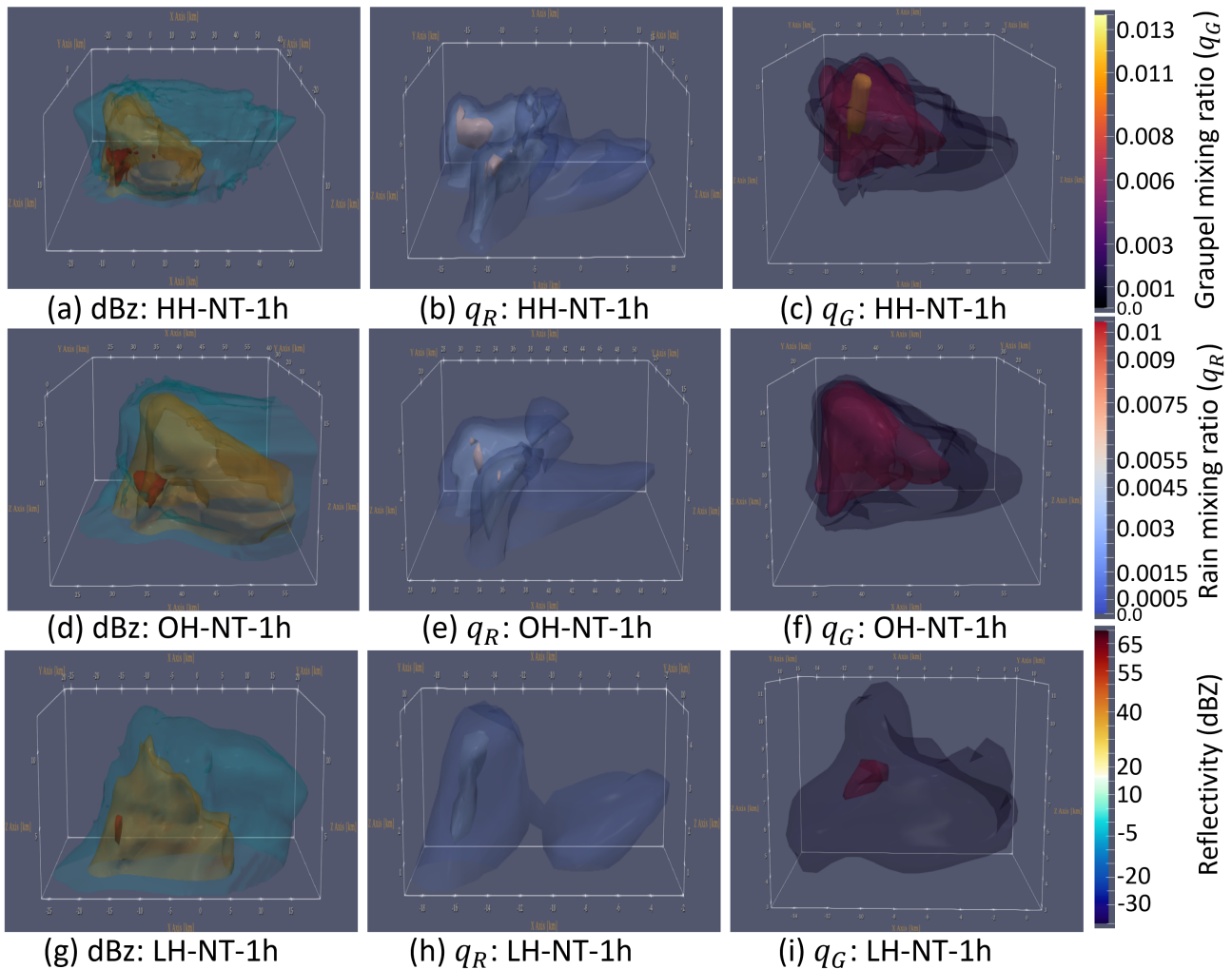
Figure 8. 3D visualization of the (top row) high-humidity (HH) (middle row) original humidity (OH), and (bottom row) low-humidity (LH) simulations without terrain (NT) for 1 hour (1h) into the simulation. Displayed are (left column) reflectivity (dBZ, contours: $-3.52, 39.72$ and 59.89 dBZ), (middle column) mixing ratio of rain (q_R in kg/kg, contours: $0.0012, 0.0035$ and 0.0069 kg/kg) and (right column) mixing ratio of graupel (q_G in kg/kg, contours: $0.0015, 0.0061$ and 0.012 kg/kg). Figure plotted with ParaView by Jose Pablo Solano Marchini.

and larger graupel or at least in accelerated development. Possibly, the effect of entrainment is larger due to the lower moisture (Rädler et al., 2018).

Overall, JPSM's project confirms the influential role of the environment on storm development, microphysical processes, and composition. This illustrates how systematic studies offer valuable insights into convective-scale processes and serve as effective educational tools.

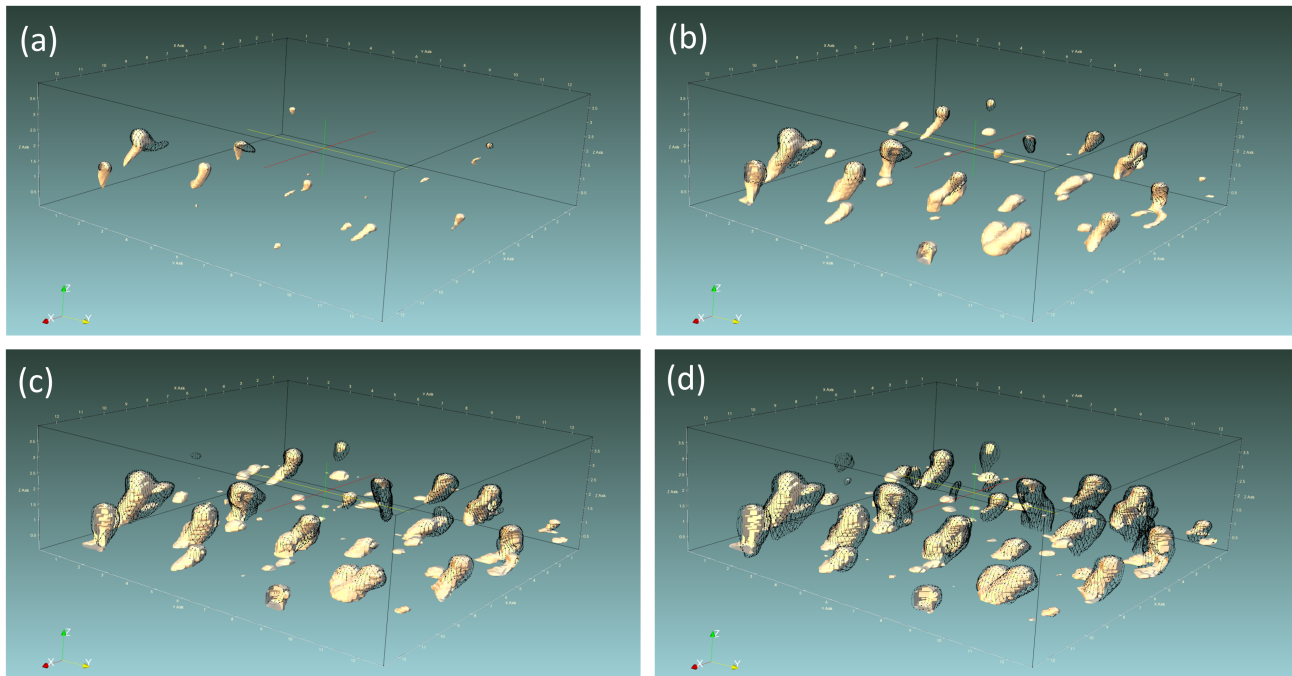## 1.4 Yidan Li's (YL) project: Visualization of precipitating and non-precipitating shallow cumulus

Figure 9. Shallow cumulus simulations at t=645 min. Displayed are different thresholds for the mixing ratio of cloud water (q_c in kg/kg, yellowish surfaces) and rain (q_R in kg/kg, black grid surfaces): (a) $q_C = 10^{-3}$, $q_r = 10^{-5}$; (b) $q_c = 10^{-4}$, $q_r = 10^{-6}$; (c) $q_c = 10^{-5}$, $q_r = 10^{-7}$ and (d) $q_c = 10^{-6}$, $q_r = 10^{-8}$. Figure plotted with ParaView by Yidan Li.

120　　YL focused on shallow cumulus instead of deep moist convection. The project is based on the paper published by van Zanten et al. (2011), who compared twelve large-eddy simulations using various microphysical representations with measurements in conjunction with the Rain in Cumulus over the Ocean (RICO) field study. They found that the ensemble of their simulations reasonably replicate observed cloud features, but the single simulations showed significant differences in microphysical structure and surface precipitation rates, particularly for simpler models. YL's project focuses on understanding changes of

125　　the microphysical composition of shallow cumulus and its potential precipitation development. She used the pre-configured CM1 simulation set-ups for shallow cumulus: les_ShallowCuPrecip and les_ShallowCu_land. However, the latter did not perform as expected and hence it is not presented here. Focus remained on shallow cumulus precipitation and on the technical aspects of the visualization. The simulation time was 24 hours with an output frequency of 5 minutes. The domain has a size of $128 \times 128 \times 100$ grid points with a horizontal grid spacing of 100 m and a vertical one of 40 m, The boundary conditions

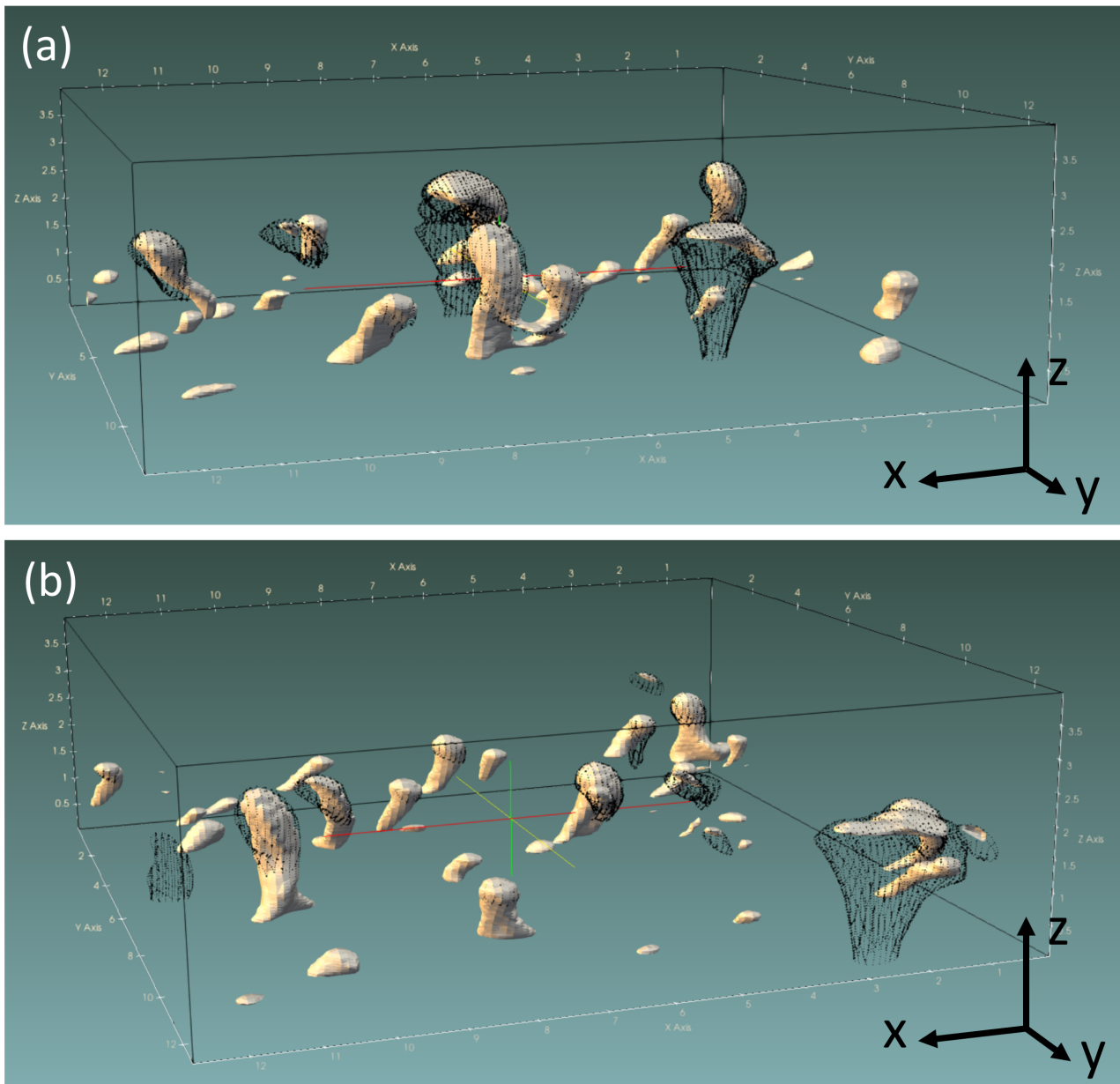130　　are periodic in x- and y-direction.

Figure 10. Shallow cumulus simulations at (a) t=930 min and (b) t=940 min. Mixing ratio of cloud water q_c is plotted as a yellowish surface for $q_c = 10^{-4}$ kg/kg; mixing ratio of rain is shown as a black mesh for $q_r = 10^{-6}$ kg/kg. Figure plotted with ParaView by Yidan Li.

In her ParaView simulations, YL explored various thresholds for cloud and rain mixing ratios q_C and q_R (refer to Fig. 9), which underscores the necessity of thoughtful selection for optimal visualizations and bears educational potential. YL

also directed her attention to technical aspects with the aim to identify the most effective methods for illuminating and color-enhancing cloud visualizations. In general, changes in cloud cover during light/heavy precipitation were challenging to observe

135 due to cloud movement. Hence, a higher output frequency would be necessary to study cloud development in even higher detail. Precipitation tended to occur in the upper part of deeper clouds.

Fig. 10 illustrates how cloud cover tends to thin during strong precipitation, confirming van Zanten et al.'s (2011) findings. Within the model framework, this process is accounted for through the conversion of cloud particles into rain particles as a result of distinct microphysical mechanisms. In Fig. 10a thicker clouds with lighter precipitation can be seen in the middle of

140 the domain and 10 minutes later (10b) the cloud has moved to the left. At the same time, clouds with a thinner cloud particle layer and with heavier precipitation are displayed towards the right of Fig. 10a,b.

In summary, YL's project serves as an example of a high-resolution, shallow-moist convective simulation, and is therefore distinct from the deep-moist convective simulations undertaken by the other students. The evolving rain and cloud particle composition of the shallow cumulus offers valuable educational insights. Moreover, the project emphasizes the importance of

145 carefully considering technical details when visualizing data.

References

Bikos, D., Weaver, J., and Motta, B.: A satellite perspective of the 3 May 1999 Great Plains tornado outbreak within Oklahoma, Weather and forecasting, 17, 635–646, https://doi.org/10.1175/1520-0434(2002)017<0635:ASPOTM>2.0.CO;2, 2002.

De Martin, F., Davolio, S., Miglietta, M. M., and Levizzani, V.: A conceptual model for the development of tornado in the Po Valley, https://doi.org/10.5194/ecss2023-17, 11th European Conference on Severe Storms, Bucharest, Romania, 8–12 May 2023, ECSS2023-17, 2023.

Hengl, T., Leal Parente, L., Krizan, J., and Bonannella, C.: Continental Europe Digital Terrain Model, https://doi.org/10.5069/G99021ZF, distributed by OpenTopography. (last-access: 2023-08-30), 2022.

Hersbach, H., Bell, B., Berrisford, P., Hirahara, S., Horányi, A., Muñoz-Sabater, J., Nicolas, J., Peubey, C., Radu, R., Schepers, D., et al.: The ERA5 global reanalysis, Quarterly Journal of the Royal Meteorological Society, 146, 1999–2049, https://doi.org/10.1002/qj.3803, 2020.

Loftus, A. M., Weber, D. B., and Doswell, C. A.: Parameterized mesoscale forcing mechanisms for initiating numerically simulated isolated multicellular convection, Monthly weather review, 136, 2408–2421, https://doi.org/10.1175/2007MWR2133.1, 2008.

Rädler, A. T., Groenemeijer, P., Faust, E., and Sausen, R.: Detecting severe weather trends using an additive regressive convective hazard model (AR-CHaMo), Journal of Applied Meteorology and Climatology, 57, 569–587, https://doi.org/10.1175/JAMC-D-17-0132.1, 2018.

Speheger, D. A., Doswell, C. A., and Stumpf, G. J.: The tornadoes of 3 May 1999: Event verification in central Oklahoma and related issues, Weather and forecasting, 17, 362–381, https://doi.org/10.1175/1520-0434(2002)017<0362:TTOMEV>2.0.CO;2, 2002.

Thompson, R. L. and Edwards, R.: An overview of environmental conditions and forecast implications of the 3 May 1999 tornado outbreak, Weather and forecasting, 15, 682–699, https://doi.org/10.1175/1520-0434(2000)015<0682:AOOECA>2.0.CO;2, 2000.

Weisman, M. L. and Klemp, J. B.: The dependence of numerically simulated convective storms on vertical wind shear and buoyancy, Monthly Weather Review, 110, 504–520, https://doi.org/10.1175/1520-0493(1982)110<0504:TDONSC>2.0.CO;2, 1982.